

Electronic phase diagram of disordered Co doped BaFe₂As₂

F. Kurth^{1,2*} and K. Iida¹, S. Trommler^{1,2}, J. Hänisch¹, K. Nenkov¹,
J. Engelmann^{1,2}, S. Oswald¹, J. Werner¹, L. Schultz^{1,2}, B. Holzapfel^{1,3}, S. Haindl^{1†}
¹*IFW Dresden, Helmholtzstr. 20, 01069 Dresden, Germany*
²*TU Dresden, 01062 Dresden, Germany*
³*TU Bergakademie Freiberg,
Akademiestr. 6, 09596 Freiberg, Germany*

Superconducting and normal state transport properties in iron pnictides are sensitive to disorder and impurity scattering. By investigation of Ba(Fe_{1-x}Co_x)₂As₂ thin films with varying Co concentration, we demonstrate that in the dirty limit the superconducting dome in the electronic phase diagram of Ba(Fe_{1-x}Co_x)₂As₂ shifts towards lower doping concentrations, which differs significantly from observations in single crystals. We show that especially in the underdoped regime superconducting transition temperatures higher than 27 K are possible.

PACS numbers: {74.70.-b, 74.62.-c, 74.25.-q}

PACS numbers: 74.70.-b, 74.62.-c, 74.25.-q

I. INTRODUCTION

Almost simultaneously with the report of superconductivity by hole doping in BaFe₂As₂,¹ Sefat *et al.* showed that also electron doping in BaFe₂As₂ is able to suppress the spin density wave (SDW) state and to stabilize superconductivity.² Since then, many studies have been devoted to an understanding of the competition between the SDW and the superconducting state in this intermetallic compound.³⁻⁸

Investigations of the electronic phase diagram of Co doped BaFe₂As₂ revealed a structural transition from a high-temperature tetragonal to a low-temperature orthorhombic phase closely above the transition from the paramagnetic to the SDW state.

With increasing doping level x in Ba(Fe_{1-x}Co_x)₂As₂ the structural and magnetic transitions split further and are suppressed.^{3,4} In addition, a characteristic superconducting dome raises with a maximal critical temperature up to $T_c = 25$ K around the optimal doping of $x = 0.06 - 0.08$ until superconductivity vanishes beyond $x = 0.18 - 0.20$. In the underdoped region ($x \leq 0.06$) superconductivity coexists with the SDW state microscopically. This extremely close vicinity of superconductivity to antiferromagnetism suggests the mediating role of spin fluctuations in the Cooper pairing.

The influence of increasing Co content in Ba(Fe_{1-x}Co_x)₂As₂ on the electronic structure results in an increase of its three-dimensionality, a gradual filling of the hole pockets near the Γ point of the Brillouin zone, and therefore a reduced nesting.⁹ It has been argued that the loss of nesting (*i.e.* the weakening of interband transitions) and the suppressed spin fluctuations are responsible for the decrease in T_c in overdoped samples, whereas in underdoped samples superconductivity has to compete with the SDW state for the carrier density.^{7,8,10,11}

A more explicit difference between the effects of electron doping on the structural, magnetic and su-

perconducting transitions was made by Canfield *et al.* by comparing Co doping with Ni and Cu doping in BaFe₂As₂.¹² They concluded that the occurrence of superconductivity depends primarily on the amount of added electrons and the c/a ratio, whereas the structural modifications, defects and magnetic phase transitions depend on the amount of added impurity ions and the c -axis parameter. In this regard other perturbations in the FeAs tetrahedral sublattice (vacancies and interstitials included) should be considered in more detail.

All the investigations mentioned above have been performed on powder samples and on single crystals. Here, we will discuss the peculiarities in the growth of Co doped BaFe₂As₂ thin films with varying Co content and the influence on the electronic phase diagram. Since the first growth of Co doped BaFe₂As₂ thin films by pulsed laser deposition (PLD),¹³⁻¹⁵ a detailed analysis of the chemical composition and homogeneity has been widely neglected. Therefore, a part of our study is devoted to the investigation of the thin film stoichiometry. Auger electron spectroscopy (AES) demonstrates that the chemical composition of the films is sensitive to the deposition conditions. One difference between thin films and single crystals of iron pnictide superconductors is their degree of disorder, easily demonstrated by RRR values. As observed in comparable films without Fe buffer, typical RRR values for Co doped BaFe₂As₂ are in the range of 1 to 2.

II. SAMPLE PREPARATION

For the preparation of the target materials the starting elements (Ba, Fe, Co and As) are mixed and mechanically milled resulting in precursor powders of Fe₂As, Co₂As, and BaAs. Precursor powders of $x = 0, 0.02, 0.04, 0.06, 0.08, 0.10, \text{ and } 0.15$ were synthesized and pressed in pellets of Ba(Fe_{1-x}Co_x)₂As₂ with different Co content. The

oxygen impurities of the starting elements were taken into account during the weighing process. Impurities in As were negligible since As was cleaned by sublimation.¹⁶ More details of the target preparation are given in appendix A.

Using the sintered $\text{Ba}(\text{Fe}_{1-x}\text{Co}_x)_2\text{As}_2$ targets, thin films with different Co concentration were fabricated by PLD under ultra high vacuum (UHV) conditions (base pressure of 10^{-9} mbar) on $\text{MgO}(100)$ substrates. A KrF excimer laser ($\lambda = 248$ nm, pulse duration = 25 ns) was used for material ablation.

Before each film deposition the target surface was cleaned by approximately 1000 laser pulses. The substrates were cleaned in an ultrasonic bath using acetone and isopropanol and subsequently transferred into the UHV chamber. A heat treatment of the substrate at 1000°C for 30 minutes followed prior to the deposition process.

Thin film growth started with the deposition of a pure Fe buffer at room temperature. The $\text{Ba}(\text{Fe}_{1-x}\text{Co}_x)_2\text{As}_2$ deposition followed at substrate temperatures between 650°C and 800°C depending on the nominal Co content (Tab. I). The deposition temperature was increased with increasing Co doping. The repetition rate was set to 5 Hz for Fe and to 10 Hz for $\text{Ba}(\text{Fe}_{1-x}\text{Co}_x)_2\text{As}_2$. Pulse numbers for the Fe buffer layer were set to 4000 - 5000 and for $\text{Ba}(\text{Fe}_{1-x}\text{Co}_x)_2\text{As}_2$ to 8000. The estimated energy densities at the target surface of $\text{Ba}(\text{Fe}_{1-x}\text{Co}_x)_2\text{As}_2$ are given in Tab. I.

III. MEASUREMENTS AND RESULTS

The phase purity of the target material was analyzed by powder X-ray diffraction (XRD) in Bragg-Brentano geometry (CoK_α radiation with $\lambda = 1.7889$ Å). Powder XRD scans of the targets and a following Rietveld analysis^{17,18} show high phase purity of the target material (the S -values for the Rietveld analysis are less than 1.3). The obtained lattice parameters follow the trend of Vegard's law and are similar to results from single crystal measurements (Fig. 1(a)).

The transition temperatures, T_c , of the processed targets were determined by SQUID and VSM measurements. The resulting phase diagram shows a maximum T_c of 23.7 K at a nominal composition $x_{\text{nom}} = 0.08$ (Fig. 1(b)).

Epitaxial growth of the thin films was confirmed by X-ray θ - 2θ scans and texture measurements as shown exemplarily in appendix B for the film grown from the $\text{Ba}(\text{Fe}_{0.92}\text{Co}_{0.08})_2\text{As}_2$ target (Fig. 6 and Fig. 7). The epitaxial relation was confirmed to be $(001)[100]\text{Ba-122}||(\text{001})[110]\text{Fe}||(\text{001})[100]\text{MgO}$.²⁰

The thickness of the Fe buffer and the $\text{Ba}(\text{Fe}_{1-x}\text{Co}_x)_2\text{As}_2$ layer was confirmed on a Focused-Ion-Beam (FIB)-cut cross section in a scanning electron microscope equipped with a FIB stage.²¹ For all films the Fe buffer thickness is between 15 and 20 nm, whereas

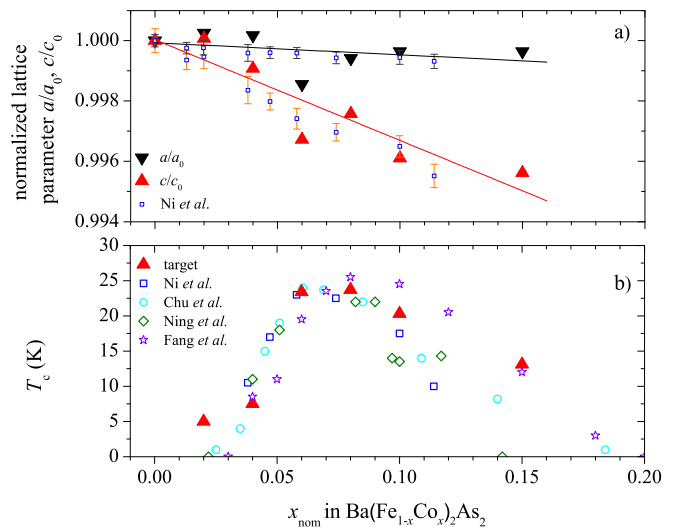


Figure 1: (a) c -axis and a -axis values of the $\text{Ba}(\text{Fe}_{1-x}\text{Co}_x)_2\text{As}_2$ target powders in dependence of the nominal doping level normalized to $x = 0$ ($a_0 = 3.96093$ Å; $c_0 = 13.01410$ Å). Linear fits are indicated by lines. The results are compared to the single crystal data from Ni *et al.*³ (small open squares). The normalized lattice parameters of the $\text{Ba}(\text{Fe}_{0.94}\text{Co}_{0.06})_2\text{As}_2$ target deviate from the linear slope. (b) Critical temperature of the target material in dependence of the Co content, compared to literature data.^{3,6,8,19}

the $\text{Ba}(\text{Fe}_{1-x}\text{Co}_x)_2\text{As}_2$ layer thickness is about 100 nm. The T_c of the samples was determined by the Van der Pauw method using a Physical Property Measurement System (PPMS). A heating rate of 1 K/min and a constant current of $100\ \mu\text{A}$ were used in the electrical transport measurements. Due to the higher conductivity of the Fe buffer layer and the resulting shunting of the current,²² the SDW anomaly in the underdoped films cannot be detected through $R(T)$ measurements. In addition, the T_c criterion (except for $T_{c,0}$) shifts towards lower resistivities and thus to lower temperatures because of the Fe buffer layer. In order to obtain the transition temperatures of the $\text{Ba}(\text{Fe}_{1-x}\text{Co}_x)_2\text{As}_2$ layer, the $R(T)$ data were corrected using the method given by S. Trommler *et al.*²²

A key question in the PLD process addresses the stoichiometric transfer of the material from the target to the substrate. Thin film stoichiometry was determined by Auger electron spectroscopy (AES) where parts of the film were sputtered and the target material was used as a standard. The resulting depth profiles of the films do not only reveal the stoichiometry but also inhomogeneities in the film compositions (Fig. 2(b)). The quantification of the film stoichiometry is based on calibrated AES measurement of target material, that was grinded and sputter cleaned using the same conditions as in the depth profiles. Thus surface contamination is removed, preferential sputtering and some

Table I: Deposition conditions and structural data of Ba(Fe_{1-x}Co_x)₂As₂ (Ba-122) /Fe bilayers.

x_{nom}	x_{AES}	dep.-temp. (°C)	energy density		φ -FWHM (°)		c -axis (Å)	$T_{c,90}$ (K)
			Ba-122 (J/cm ²)	Fe (J/cm ²)	Ba-122 (103)	Fe (110)		
0	0	650	2.45	2.85	1.82	1.23	12.99775	
0.02	0.015	700	2.50	3.10	1.23	1.04	12.93307	13.0
0.04	0.035	750	2.65	3.30	0.78	0.75	12.79980	27.9
0.06	0.049	750	2.75	3.05	0.81	0.87	12.85912	27.5
0.08	0.075	750	2.50	2.60	0.81	0.80	12.84935	24.7
0.10	0.107	750	2.75	3.15	0.99	1.11	12.82454	20.6
0.15	0.134	800	2.75	3.15	1.14	0.81	12.74101	22.1
0.15	0.132	750	2.50	2.50	1.27	0.87	12.78704	20.3

peak interferences (signals of Ba partly overlapped by Fe) are considered in the concentration quantification of the layers. The Ba-122 target material with a doping of $x_{\text{nom}} = 0.1$ assumed to be in nominal stoichiometry was used to create a set of sensitivity factors for calibration, confirmed also for the $x_{\text{nom}} = 0.02$ target material. The calibration thus works well in the Ba(Fe_{1-x}Co_x)₂As₂ layer of the films, but cannot be used for quantification in the Fe buffer layer.

A remarkable observation is the As deficiency especially in underdoped films compared to the target material. The maximum As deficiency is estimated from AES to be about $\delta = 0.15$ in Ba(Fe_{1-x}Co_x)₂As_{2- δ} (Fig. 2(a)). We assume As diffusion into the Fe buffer during film growth. Additionally, diffusion of Co into the Fe buffer layer is noticeable, and its amount changes with varying Co content and deposition temperatures. In the higher doped samples with a nominal Co content of $x_{\text{nom}} = 0.15$ a large Co gradient over the layer thickness was found for increased deposition temperatures. A diffusion of Co into the Fe buffer layer takes place especially at elevated temperatures where the Co content in the Fe buffer increases. The Co content in Ba(Fe_{1-x}Co_x)₂As₂ thin films deposited at higher temperatures ranges between $x = 0.20$ and $x = 0.09$. A steep Co concentration gradient along the film thickness as well as a strong Co diffusion into the Fe buffer can be observed. In contrast, the Co gradient of the thin film and the Co diffusion into the Fe buffer deposited at 750 °C is significantly smaller (Fig. 2(b)). Despite local inhomogeneities, the measured Co concentration, x_{AES} , in the thin films follows the nominal Co content x_{nom} quite well (Fig. 3).

The c -axis lattice parameter of the Ba(Fe_{1-x}Co_x)₂As₂ phase decreases with increasing x_{AES} (Fig. 4 (a)). The c -axis of the thin films is always smaller compared to the c -axis of the bulk targets. The resulting electronic phase diagram determined from the thin films is shown in Fig. 4(b). The error bars in x_{AES} indicate the difference between the highest and the lowest doping value determined by AES. The error bars in T_c show the transition width of the corrected measurements from $T_{c,90}$ to $T_{c,10}$ ($T_{c,90}$ and the $T_{c,10}$ being taken at 90 % and 10 % of the normal state resistivity at 35 K).

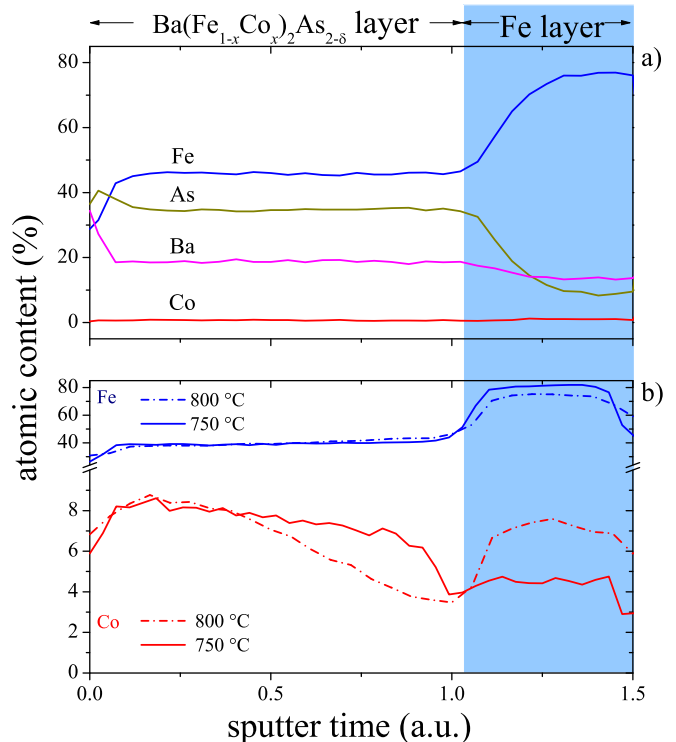


Figure 2: (a) AES result of the Ba(Fe_{0.98}Co_{0.02})₂As_{2- δ} thin film. The As deficiency in the Ba(Fe_{0.98}Co_{0.02})₂As_{2- δ} layer shows up to $\delta = 0.15$ (b) Co dopant and Fe concentrations in the nominal Ba(Fe_{0.85}Co_{0.15})₂As₂ and the Fe layer for different deposition temperatures, 750 °C (solid lines) and 800 °C (dash-dotted lines).

IV. DISCUSSION

The measured Fe/Co ratio indicates a qualitative agreement between nominal and measured concentrations (Fig. 3). In all thin films, As deficiency was observed with approximately $\delta = 0.25$ (Fig. 2(a)). Quantitatively, the stoichiometric transfer from the target to the thin film cannot be exactly determined from our analysis yet.

Simultaneously, we have observed a Co concentration

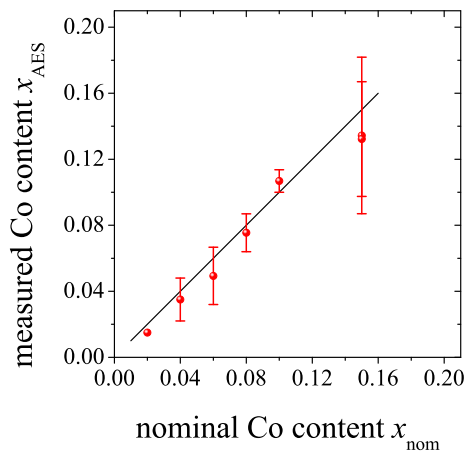


Figure 3: The doping x_{AES} measured by AES in the thin films compared to the nominal Co content x_{nom} .

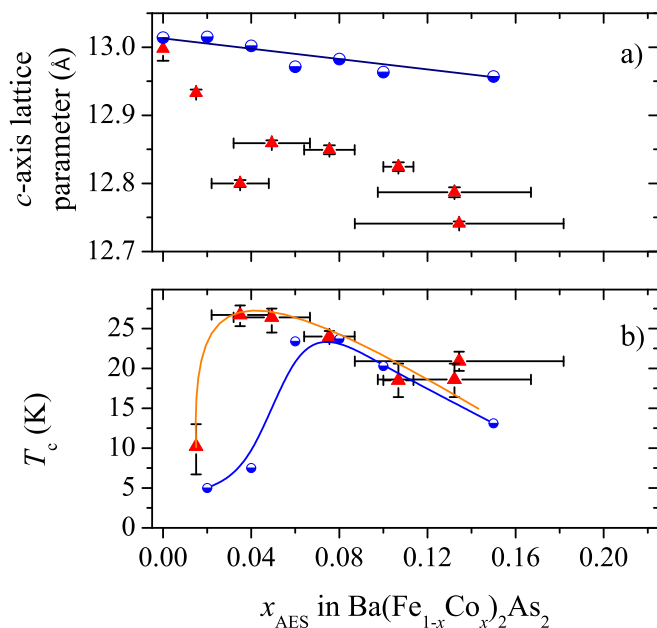


Figure 4: (a) c -axis values for thin films with different Co content, x . (b) The phase diagram of the Co doped BaFe_2As_2 thin films (red). The error in T_c is given by the values for $T_{c,90}$ and $T_{c,10}$ and hence the transition width. The error bars for the Co doping represent the Co gradient measured by AES. The blue dots represent the data points of the bulk material, used for PLD.

gradient along the film cross section for films with a high Co doping level. At elevated deposition temperatures, Co easily diffuses into the Fe buffer. The resulting gradient of the Co dopant in BaFe_2As_2 is responsible for a sequence of differently doped regions along the thickness. Instead of a homogeneously overdoped film, there are also optimally Co doped layers which may be responsible for a higher T_c compared to bulk values in the electronic phase diagram.

The explanation for the enhanced T_c values in underdoped films is more subtle. The Co concentration gradient is less pronounced (Fig. 2(a)), hence, it cannot be considered as primary candidate for the high T_c values. Strain effects cannot be excluded completely, however, a quantification is still missing. In addition, the role of the Fe buffer layer between substrate and iron pnictide thin film is yet unclear. First, the buffer layer is supposed to act as strain absorber. Second, it has to be further investigated how its ferromagnetism influences the SDW and/or the superconducting state of BaFe_2As_2 due to proximity.

Instead of strain we propose disorder as primary candidate to explain the observed T_c enhancement. Impurities in superconductors (one aspect of disorder) are generally classified according to their scattering potential as magnetic or non-magnetic and act as Cooper pair breaker leading to a T_c suppression described by the Abrikosov-Gor'kov formula in conventional superconductors.²³ The situation is more complex in multiband superconductors, where the effects of impurity scattering are dependent on the scattering strength and the anisotropy of the scattering potential, the coupling constant matrix, the symmetry of the superconducting gap (s^\pm , s^{++} , d -wave), and, finally the scattering channels commonly denoted as intraband and interband.²⁴

In the case of underdoped $\text{Ba}(\text{Fe}_{1-x}\text{Co}_x)_2\text{As}_2$, superconductivity coexists microscopically with a SDW state, *i.e.* SDW and superconductivity compete for the same electrons.^{10,11} Shifting the superconducting dome in the electronic phase diagram is thus a result of any mechanism suppressing the SDW but leaving the Cooper pairing intact.

A very recent theoretical work proposes that non-magnetic impurity scattering suppresses the SDW transition more strongly than the superconducting transition. Thus it is responsible for an enhancement of T_c in underdoped $\text{Ba}(\text{Fe}_{1-x}\text{Co}_x)_2\text{As}_2$.²⁵ This was experimentally demonstrated by additional Cu doping of $\text{Ba}(\text{Fe}_{1-x}\text{Co}_x)_2\text{As}_2$.²⁶ Under the assumption of s^\pm pairing^{27,28} and a dominant intraband impurity scattering, the superconducting state survives but at the same time the SDW state is weakened.²⁵

The same argument, however, holds for any additional (non-magnetic or magnetic) intraband scattering in the hole pocket^{24,29,30} that acts detrimentally on the SDW formation without strong influence on (s^{++} or s^\pm) superconductivity. This might be the case for the thin films investigated here, where we suggest As vacancies acting as active impurities. Although As vacancies may be primarily regarded as non-magnetic defects, they are also able to form localized magnetic moments.^{31,32} Similarly, Se vacancies have been reported to act as magnetic defects in $\text{FeSe}_{1-\delta}$.³³ Investigations of As deficient oxy-pnictides found a ferromagnetically ordered Fe cluster around As vacancies³⁴⁻³⁷ which does not suppress T_c . A magnetic impurity scattering contribution due to As vacancies would favour s^\pm pairing in the $\text{Ba}(\text{Fe}_{1-x}\text{Co}_x)_2\text{As}_2$

thin films. However, in the *dirty limit* a crossover from s^\pm to s^{++} is also possible.

In addition, Cvetkovic and Tesanovic³⁸ have argued that the itinerant character of the FeAs tetrahedral sublattice is reduced with increased flattening. The c -axis lattice constants of $\text{Ba}(\text{Fe}_{1-x}\text{Co}_x)_2\text{As}_2$ thin films are drastically smaller compared to the bulk samples. This structural modification might be responsible for a further stabilization of Cooper pairing in the underdoped regime, however, more systematic results are required in order to qualify and quantify strain effects.

V. CONCLUSIONS

To summarize, we have studied the superconducting transition in the electronic phase diagram of Co doped BaFe_2As_2 thin films prepared by PLD. The thin films allow to study the effect of disorder and superconductivity in the *dirty limit*. We have reported a significant effect on the electronic phase diagram: the measured T_c values are higher compared to single crystal data, and the superconducting dome shifts towards lower Co content. The highest $T_{c,90}$ of 27.9 K was achieved at $x_{\text{AES}} = 0.035 (\pm 0.013)$. Generally, this change in the electronic phase diagram for Co doped BaFe_2As_2 thin films can qualitatively be understood by taking into account disorder effects and impurity scattering. Additional (non-magnetic or magnetic) intraband scattering weakens the SDW but has less effect on the superconducting state. The thin films in this work are As deficient compared to single crystals. We thus propose As vacancies as a possible candidate for additional intraband scattering centers in Co doped BaFe_2As_2 being responsible for a suppression of the SDW in favour of Cooper pairing. A more detailed analysis of the role of As vacancies as impurity scatterers in Co doped BaFe_2As_2 is currently under investigation. Strain and the influence of the ferromagnetic Fe buffer layer may have similar effects on SDW and superconductivity. Their contribution is unclear and cannot yet be separated or quantified completely. Finally, due to the high complexity of disorder effects and impurity scattering in multiband superconductivity as well as the coexistence of superconductivity with a SDW state, the term *dirty limit* in the iron pnictides may describe qualitatively quite different scenarios and its meaning for superconducting properties has to be specified carefully.

ACKNOWLEDGMENTS

The authors acknowledge the financial support under the HA 5934/3-1 (SPP 1458) from the German Research Foundation. F. Kurth acknowledges financial support of the EU (Iron-Sea under project No. FP7-283141). The authors thank S.-L. Drechsler, E. Reich, A. Reisner, V. Grinenko, and R. Hühne for valuable discussions as well as U. Besold and M. Kühnel for technical support. The

work was carried out at IFW Dresden.

Appendix A: Target Preparation

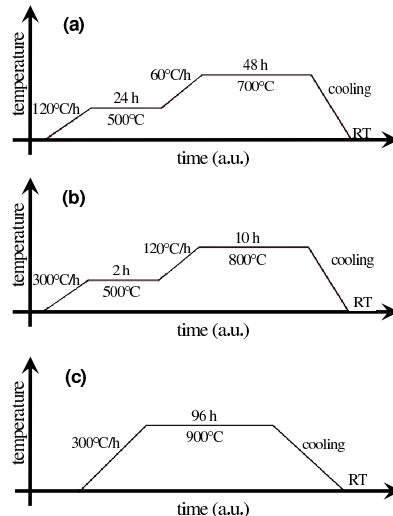
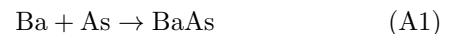


Figure 5: (a) Heat treatment for BaAs, (b) for Co_2As and Fe_2As , and (c) for $\text{Ba}(\text{Fe}_{1-x}\text{Co}_x)_2\text{As}_2$.

For the preparation of the BaAs precursor a two-zone quartz ampoule was used to guarantee a safe solid state reaction under Ar-shielding gas atmosphere. Prior to this, the ampoule was baked out under vacuum for 10 h at 500 °C to remove contaminations. The heat treatment for the reaction

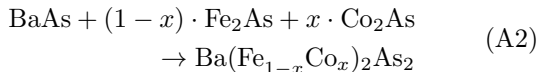


is shown in Fig. 5(a) and consists of a heating ramp (120 °C/h), and a holding step at 500 °C for 24 h. Afterwards the heating continued with a rate of 60 °C/h up to 700 °C above the sublimation point of As. BaAs was held at this temperature for 48 h before cooling down to room temperature with a fast rate of 600 °C/h.

For the production of Fe_2As and Co_2As , mechanically milled elements with a homogeneous grain size of 100 μm were used. Fe and As as well as Co and As were mixed under consideration of oxygen impurities in the ratio of 2:1, respectively.

All milled powders were pressed to cylindrically shaped pellets with a diameter of 10 mm by the use of a hydraulic press (Perkin Elmer) with a pressure of $12 \cdot 10^6 \text{ N/m}^2$. The pellets were placed in a quartz ampoule, and the heat treatment took place under Ar shielding gas. After a heating to 500 °C with a rate of 300 °C/h the temperature was held for 2 h. A further ramp to 800 °C with a rate of 120 °C and a holding time of 10 h followed. The pellets were cooled down to room temperature (Fig. 5(b)).

Finally, after milling, mixing via the reaction



and pressing the powder material to pellets with a diameter of 10 mm, $\text{Ba}(\text{Fe}_{1-x}\text{Co}_x)_2\text{As}_2$ was synthesized according to the heat treatment given in Fig. 5(c).

Appendix B: XRD data for thin films

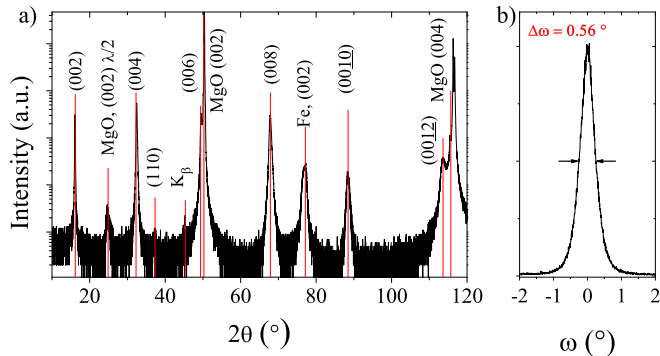


Figure 6: (a) $\theta - 2\theta$ scan of the thin film grown from a $\text{Ba}(\text{Fe}_{0.92}\text{Co}_{0.08})_2\text{As}_2$ target (b) Rocking curve of the $\text{Ba}(\text{Fe}_{0.92}\text{Co}_{0.08})_2\text{As}_2$ (004) reflection c -axis showing the highly c -axis textured growth of the film.

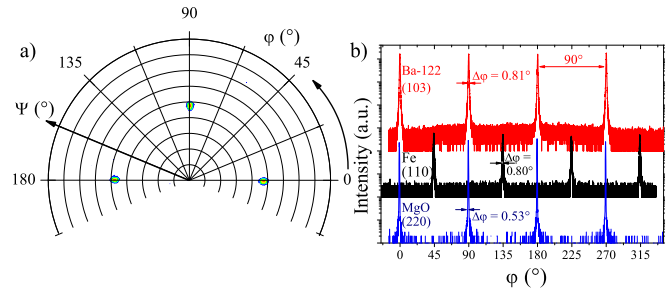


Figure 7: (a) Pole figure of the $\text{Ba}(\text{Fe}_{0.92}\text{Co}_{0.08})_2\text{As}_2$ (103) reflection, (b) MgO, Fe and $\text{Ba}(\text{Fe}_{0.92}\text{Co}_{0.08})_2\text{As}_2$ φ -scan.

Exemplarily the XRD thin film data and the texture data are given by Fig. 6 and Fig. 7. The full width at half maximum (FWHM) of the φ -scans of the $\text{Ba}(\text{Fe}_{1-x}\text{Co}_x)_2\text{As}_2$ (103) reflection is between 0.78° and 1.82° (Tab. I). These values are not corrected for device broadening. Applying the Nelson-Riley extrapolation for θ - 2θ scans, the c -axes of the thin films were determined. Within the doping series, the c -axis lattice parameters follow Vegard's law (Fig. 4).

The pole figure of the $\text{Ba}(\text{Fe}_{0.92}\text{Co}_{0.08})_2\text{As}_2$ (103) reflection and the φ -scans of the $\text{Ba}(\text{Fe}_{0.92}\text{Co}_{0.08})_2\text{As}_2$, the Fe (110) and the MgO (220) reflection are presented in Fig. 7(a) and 7(b) and demonstrate the epitaxial relation between film and substrate.

* Fritz.Kurth@ifw-dresden.de

† S.Haindl@ifw-dresden.de

¹ M. Rotter, M. Tegel, and D. Johrendt, Phys. Rev. Lett. **101**, 107006 (2008).

² A. S. Sefat, R. Jin, M. A. McGuire, B. C. Sales, D. J. Singh, and D. Mandrus, Phys. Rev. Lett. **101**, 117004 (2008).

³ N. Ni, M. E. Tillman, J.-Q. Yan, A. Kracher, S. T. Hannahs, S. L. Bud'ko, and P. C. Canfield, Phys. Rev. B **78**, 214515 (2008).

⁴ J.-H. Chu, J. G. Analytis, D. Press, K. De Greve, T. D. Ladd, Y. Yamamoto, and I. R. Fisher, Phys. Rev. B **81**, 214502 (2010).

⁵ P. Marsik, K. W. Kim, A. Dubroka, M. Rössle, V. K. Malik, L. Schulz, C. N. Wang, C. Niedermayer, A. J. Drew, M. Willis, T. Wolf, and C. Bernhard, Phys. Rev. Lett. **105**, 057001 (2010).

⁶ F. Ning, K. Ahilan, I. Imai, A. S. Sefat, R. Jin, M. A. McGuire, B. C. Sales, and D. Mandrus, J. Phys. Soc. Jpn **78**, 013711 (2009).

⁷ F. L. Ning, K. Ahilan, T. Imai, A. S. Sefat, M. A. McGuire, B. C. Sales, D. Mandrus, P. Cheng, B. Shen, and H.-H.

Wen, Phys. Rev. Lett. **104**, 037001 (2010).

⁸ L. Fang, H. Luo, P. Cheng, Z. Wang, Y. Jia, G. Mu, B. Shen, I. I. Mazin, L. Shan, C. Ren, and H.-H. Wen, Phys. Rev. B **80**, 140508 (2009).

⁹ S. Thirupathaiah, S. de Jong, R. Ovsyannikov, H. A. Dürr, A. Varykhalov, R. Follath, Y. Huang, R. Huisman, M. S. Golden, Y.-Z. Zhang, H. O. Jeschke, R. Valentí, A. Erb, A. Gloskovskii, and J. Fink, Phys. Rev. B **81**, 104512 (2010).

¹⁰ A. D. Christianson, M. D. Lumsden, S. E. Nagler, G. J. MacDougall, M. A. McGuire, A. S. Sefat, R. Jin, B. C. Sales, and D. Mandrus, Phys. Rev. Lett. **103**, 087002 (2009).

¹¹ D. K. Pratt, W. Tian, A. Kreyssig, J. L. Zarestky, S. Nandi, N. Ni, S. L. Bud'ko, P. C. Canfield, A. I. Goldman, and R. J. McQueeney, Phys. Rev. Lett. **103**, 087001 (2009).

¹² P. C. Canfield, S. L. Bud'ko, N. Ni, J. Q. Yan, and A. Kracher, Phys. Rev. B **80**, 060501 (2009).

¹³ K. Iida, J. Hänisch, R. Hühne, F. Kurth, M. Kiszun, S. Haindl, J. Werner, L. Schultz, and B. Holzapfel,

- Appl. Phys. Lett. **95**, 192501 (2009).
- ¹⁴ S. Lee, J. Jiang, J. D. Weiss, C. M. Folkman, C. W. Bark, C. Tarantini, A. Xu, D. Abraimov, A. Polyanskii, C. T. Nelson, Y. Zhang, S. H. Baek, H. W. Jang, A. Yamamoto, F. Kametani, X. Q. Pan, E. E. Hellstrom, A. Gurevich, C. B. Eom, and D. C. Larbalestier, Appl. Phys. Lett. **95**, 212505 (2009).
- ¹⁵ T. Katase, H. Hiramatsu, H. Yanagi, T. Kamiya, M. Hirano, and H. Hosono, Solid State Commun. **149**, 2121 (2009).
- ¹⁶ H. Briehl, *Chemie der Werkstoffe* (Teubner B.G. GmbH, 1995).
- ¹⁷ H. M. Rietveld, *The Rietveld Method*, Tech. Rep. ECN-RX-90-035 (Energy Research Foundation, Petten, The Netherlands, 1990).
- ¹⁸ J. Rodriguez-Carvajal, *Structural Analysis from Powder Diffraction Data: The Rietveld Method*, Tech. Rep. (Laboratoire Léon Brillouin, 2001).
- ¹⁹ J.-H. Chu, J. G. Analytis, C. Kucharczyk, and I. R. Fisher, Phys. Rev. B **79**, 014506 (2009).
- ²⁰ T. Thersleff, K. Iida, S. Haindl, M. Kidszun, D. Pohl, A. Hartmann, F. Kurth, J. Hänisch, R. Hühne, B. Rellinghaus, L. Schultz, and B. Holzapfel, Appl. Phys. Lett. **97**, 022506 (2010).
- ²¹ K. Iida, S. Haindl, T. Thersleff, J. Hänisch, F. Kurth, M. Kidszun, R. Hühne, I. Mönch, L. Schultz, B. Holzapfel, and R. Heller, Appl. Phys. Lett. **97**, 172507 (2010).
- ²² S. Trommler, R. Hühne, J. Hänisch, E. Reich, K. Iida, S. Haindl, V. Matias, L. Schultz, and B. Holzapfel, Appl. Phys. Lett. **100**, 122602 (2012).
- ²³ A. Abrikosov and L. Gor'kov, Zhur. Eksptl'. i Teoret. Fiz. **Vol: 39**, 1781 (1960).
- ²⁴ A. A. Golubov and I. I. Mazin, Phys. Rev. B **55**, 15146 (1997).
- ²⁵ R. M. Fernandes, M. G. Vavilov, and A. V. Chubukov, Phys. Rev. B **85**, 140512 (2012).
- ²⁶ N. Ni, A. Thaler, J. Q. Yan, A. Kracher, E. Colom-bier, S. L. Bud'ko, P. C. Canfield, and S. T. Hannahs, Phys. Rev. B **82**, 024519 (2010).
- ²⁷ I. I. Mazin, D. J. Singh, M. D. Johannes, and M. H. Du, Phys. Rev. Lett. **101**, 057003 (2008).
- ²⁸ K. Kuroki, S. Onari, R. Arita, H. Usui, Y. Tanaka, H. Kontani, and H. Aoki, Phys. Rev. Lett. **101**, 087004 (2008).
- ²⁹ A. V. Chubukov, D. V. Efremov, and I. Eremin, Phys. Rev. B **78**, 134512 (2008).
- ³⁰ M. L. Kulić, S.-L. Drechsler, and O. V. Dolgov, EPL (Europhysics Letters) **85**, 47008 (2009).
- ³¹ K. Kikoin and S.-L. Drechsler, J Magn Magn Mater (2012), 10.1016/j.jmmm.2012.02.068.
- ³² K. Kikoin, S.-L. Drechsler, J. Malek, and J. van den Brink, (unpublished).
- ³³ K.-W. Lee, V. Pardo, and W. E. Pickett, Phys. Rev. B **78**, 174502 (2008).
- ³⁴ G. Fuchs, S.-L. Drechsler, N. Kozlova, G. Behr, A. Köhler, J. Werner, K. Nenkov, R. Klingeler, J. Hamann-Borrero, C. Hess, A. Kondrat, M. Grobosch, A. Narduzzo, M. Knupfer, J. Freudenberger, B. Büchner, and L. Schultz, Phys. Rev. Lett. **101**, 237003 (2008).
- ³⁵ G. Fuchs, S.-L. Drechsler, N. Kozlova, M. Bartkowiak, J. E. Hamann-Borrero, G. Behr, K. Nenkov, H.-H. Klauss, H. Maeter, A. Amato, H. Luetkens, A. Kwadrin, R. Khasanov, J. Freudenberger, A. Köhler, M. Knupfer, E. Arushanov, H. Rosner, B. Büchner, and L. Schultz, New Journal of Physics **11**, 075007 (2009).
- ³⁶ V. Grinenko, K. Kikoin, S.-L. Drechsler, G. Fuchs, K. Nenkov, S. Wurmehl, F. Hammerath, G. Lang, H.-J. Grafe, B. Holzapfel, J. van den Brink, B. Büchner, and L. Schultz, Phys. Rev. B **84**, 134516 (2011).
- ³⁷ F. Hammerath, S.-L. Drechsler, H.-J. Grafe, G. Lang, G. Fuchs, G. Behr, I. Eremin, M. M. Korshunov, and B. Büchner, Phys. Rev. B **81**, 140504 (2010).
- ³⁸ V. Cvetkovic and Z. Tesanovic, EPL (Europhysics Letters) **85**, 37002 (2009).